ACS APPLIED MATERIALS & INTERFACES

www.acsami.org

Research Article

Cathode–Anode Spatial Division Photoelectrochemical Platform Based on a One-Step DNA Walker for Monitoring of miRNA-21

Chuan Huang,[§] Yunqing Liu,[§] Yina Sun, Fengyi Wang, Shenguang Ge,* and Jinghua Yu

Cite This: *ACS Appl. Mater. Interfaces* 2021, 13, 35389–35396

Read Online

ACCESS | Metrics & More | Article Recommendations | Supporting Information

ABSTRACT: Photoelectrochemical (PEC) biosensors carried out the whole reaction process in the same solution, which would limit the sensitivity and selectivity of detection in the sensing system. Herein, we reported a promising new cathode–anode spatial division PEC platform based on the two-electrode synergistic enhancement strategy. With the photoanode and photocathode integrated in the same current circuit, the platform exhibited an increased photocurrent response, as well as an improved anti-interference ability led by separating the two electrodes spatially. In this proposal, red light-driven $AgInS_2$ nanoparticles (NPs) served as the photoanode to build biometric steps and amplify the signal, whereas p-type PbS quantum dots were selected as the photocathode to increase the signal. With the participation of alkaline phosphatase (ALP) labeled on Au NPs–DNA, ascorbic acid 2-phosphate was catalyzed to produce ascorbic acid as an electron donor, resulting in the enhancement of the PEC signal. Interestingly, in the presence of miRNA-21 and T7 Exo, the one-step DNA walker amplification can be triggered to reduce the PEC signal by releasing ALP-Au NP–DNA. The constructed PEC biosensor exhibited a detection limit of as low as 3.4 fM for miRNA-21, which was expected to be applied to early clinical diagnosis. Also, we believe that the proposed cathode–anode spatial division PEC platform can open up a new view for the establishment of other types of PEC biosensors.

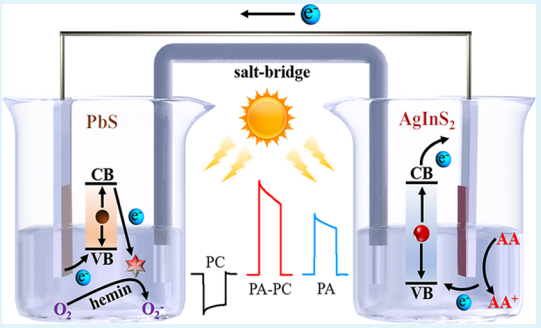

KEYWORDS: *photoelectrochemical, DNA walker, MicroRNA-21, $AgInS_2$, PbS*

1. INTRODUCTION

MicroRNAs (miRNAs) are a type of noncoding, small-molecule, single-stranded RNAs that have the function of regulating gene expression at the translation level.[1,2] Mounting evidence has demonstrated that miRNAs are closely related to tumor formation and metastasis and can be used to identify the degree of cell expression of proto-oncogenes in the human body. According to the literature reports, abnormal fluctuations in miRNA-21 expression levels were detected in various tumor specimens as well as cell lines, including breast, cervical, lung, pancreatic, prostate, colorectal, glial, and cholangiocarcinoma.[3,4] Since miRNA-21 is a recognized carcinogenic RNA, its sensitive and specific detection has become an urgent research topic.

Among various miRNA analytical methods, the photoelectrochemical (PEC) technique has attracted extensive attention due to its versatility, high sensitivity, simple equipment, and so forth.[5−8] Benefiting from facile preparation, easy modification, high photochemical activity, and stability, the previous works have mainly focused on photoanodic biosensors with n-type semiconductor-sensitized materials such as TiO_2, $BiVO_4$, CdS quantum dots (QDs), and so on.[9−13] The n-type semiconductor took electrons as the main carriers and inclined to interact with electron donors to produce a significant photocurrent response.[14,15] As a typical ternary n-type semiconductor material, $AgInS_2$ exhibited fast charge conduction rate under red-light excitation.[16,17] Nevertheless, the photoanodic biosensors suffered from insufficient anti-interference performance. The coexisting reducing components in actual samples (such as H_2O_2,[18] dopamine, and nicotinamide adenine dinucleotide,[19,20] etc.) would compete with the original electron donor, leading to the unpredictable photocurrent response, thereby limiting the clinical application of such photoanodes. More importantly, the entire reaction system of photoanodic biosensors in the past was limited in the same reaction solution, and redox side reactions on the counter electrode during the sensing process would inevitably affect the accuracy of the detection results. Apparently, improving the selectivity of photoanodes could not rely solely on the choice of n-type semiconductors. To improve the selectivity of PEC sensors, recent research had been focused on p-type semiconductors and the corresponding photocathodes, involving Cu_2O, NiO, CdTe, GaAs, $CuInS_2$, and so forth.[21−24] PbS was

Received: May 6, 2021
Accepted: July 14, 2021
Published: July 22, 2021

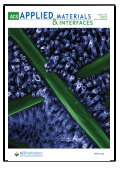

an intriguing p-type semiconductor with near-infrared light absorption, which exhibited multiple exciton generation.[25,26] The p-type semiconductor with rich hole concentration tended to interact with electron acceptors rather than electron donors, which means that the corresponding photocathodic biosensors overcome the interference of reducing substances in complex biochemical samples.[27] The increase in selectivity made the photocathodic biosensors capable of accurately detecting the real sample, which possessed the value of clinical application.[28] Unfortunately, compared with the electron donor, the electron acceptor did not have obvious promotional effect in the PEC conversion, resulting in poor photocurrent response and low detection sensitivity of the photocathode dominated by hole conduction. Similarly, the previously studied photocathodic biosensors did not overcome the disadvantage that the entire detection system was in the uniform electrolyte, which affected the anti-interference ability.

The traditional PEC biosensor using a single photoelectrode signal amplification still had shortcomings, in which the counter electrode only served as a connection to the circuit, and side reactions on the surface might even interfere with the testing consequences.[29] In order to amplify the photocurrent signal and eliminate the influence of the coexisting electrode, the counter electrode was creatively replaced with a photoelectrode. The spatial division between the photoanode and the photocathode was further realized by being placed in different electrolyte solutions and linked by a salt bridge. Based on the two-electrode synergistic enhancement strategy,[30] the cathode−anode spatial division PEC platform could be simultaneously excited by light to generate electron−hole pairs, and the above two electrodes promoted each other in the same loop, thereby greatly improving the photocurrent response. While retaining the advantages of the photocathode and photoanode, the cathode−anode spatial division PEC platform also eliminated the mutual interference between the two electrodes, which could greatly improve the detection sensitivity and specificity.

In this work, $AgInS_2$ nanoparticles (NPs) with excellent hydrophilicity and biocompatibility were selected as the photoanode to build one-step DNA walker amplification. The unique mechanical motion characteristics of the DNA walker could be applied to the directional conduction and amplification of detection signals, thus showing broad application prospects in the field of analysis and sensing,[31−34] whereas PbS QDs with long excited-state lifetimes were picked as the photocathode, which made the photoinduced electron transfer between QDs and redox species easier. Hence, hemin was added to the electrolyte in the photocathode region to increase the cathode photocurrent,[20] that is, indirectly to increase the total initial photocurrent, and thus improved the sensitivity of detection. With the photoanode and photocathode integrated in the same current circuit, the proposed PEC biosensor exhibited an increased photocurrent response, as well as an improved anti-interference ability led by separating the two electrodes spatially. Since the integration and spatial division of the photoanode and photocathode greatly improved the sensitivity and selectivity of detection respectively, the platform realized the sensitive and specific detection of miRNA-21 and opened up new areas for the construction of other types of PEC biosensors.

2. EXPERIMENTAL SECTION

2.1. Materials and Apparatus. The materials and apparatus are described in Supporting Information.

2.2. Synthesis of $AgInS_2$ NPs. Mercaptopropionic acid (MPA)-capped $AgInS_2$ NPs were synthesized according to the previously reported method with appropriate modifications.[16] In brief, after dissolving 1 mmol of $AgNO_3$ and 2 mmol of indium (III) acetate in 9 mL of ethylene glycol orderly, 1220 μL of MPA was added dropwise and stirred for 10 min under argon to form a homogeneous solution. Immediately afterward, the reaction mixture was heated to 150 °C under an argon atmosphere for 30 min and naturally cooled to room temperature. Subsequently, the sample was centrifuged and washed with ultrapure water three times, dried in an oven, and collected for further use. To prepare the working electrode, the fluorine-doped tin oxide (FTO) electrode was ultrasonically treated with acetone, ethanol, and ultrapure water in sequence. Finally, 10 μL of 5 mg/mL stable MPA-capped $AgInS_2$ NP aqueous suspension was added dropwise onto the FTO conductive surface and dried at 37 °C.

2.3. Preparation of PbS QDs. Thioglycolic acid (TGA)-stabilized PbS QDs were prepared according to the reported literature with slight modifications.[20] First, 25 mL of 4.0 mM $Pb(NO_3)_2$ aqueous solution was mixed with 17 μL of TGA thoroughly, followed by addition of 1.0 M NaOH dropwise to adjust the pH to 11. Accordingly, the solution changed from turbid to clear. After purging and removing oxygen with high-purity argon for 30 min, 2.0 mL of 0.015 M Na_2S was injected into the above clear solution. The solution changed from colorless to dark brown, which proved the initial formation of PbS QDs. Subsequently, the resulting mixture solution was maintained under an argon atmosphere for 4 h to obtain TGA-stabilized PbS QDs. Finally, the cleaned FTO was alternately immersed in a 2% poly-(diallyldimethylammonium chloride) (PDDA) solution containing 0.5 M NaCl and the previously obtained TGA-stabilized PbS QD solution for 10 min, which was repeated three times to form a stable PDDA/PbS multilayer film.[35] The films were discreetly washed with ultrapure water after each dipping step.

2.4. Synthesis of the ALP-Au NP−DNA Conjugates. First, 0.2 M K_2CO_3 was added dropwise to adjust the pH of the Au NP solution to 8.2 under stirring. Second, substrate−DNA (20 μL, 20 μM) and alkaline phosphatase (ALP) (40 μL, 0.8 mg/mL) were sequentially added to 2.0 mL of alkaline Au NP solution, incubated for 2 h, and then blocked nonspecific sites with 200 μL of 6-mercaptohexanol solution (2 mM) for 30 min at room temperature. Next, the solution mixture was centrifuged at 10,000 rpm for 20 min and washed several times to remove residues. Finally, the obtained ALP-Au NP−DNA conjugates were dissolved in 200 μL of ultrapure water for further use.

2.5. Fabrication of the miRNA-21 PEC Biosensor. Above all, DNA1 oligonucleotide (10 μL, 2 μM) and DNA2 oligonucleotide (10 μL, 1 μM) were dissolved in 80 μL of the buffer. Subsequently, the mixture solution was heated to 95 °C for 5 min and naturally cooled to room temperature to form a composite structure, that is, a DNA swing arm. Then, 10 μL of the DNA swing arm solution was incubated on the $AgInS_2$ NP-modified photoanode for 12 h at 4 °C. Next, the modified electrode was incubated with 10 μL of ALP−AuNP−DNA conjugates for 3 h at 4 °C. After that, the electrode was covered with 10 mM monoethanolamine (MEA) for 2 h to block nonspecific adsorption sites. Finally, 10 μL of the reaction solution consisting of 1× NE buffer 4, target miRNA-21, and 100 U/mL T7 Exo were added dropwise on the modified biosensing electrode to incubate for 4 h at 25 °C. The electrode surface was rinsed with the buffer to eliminate unstable residues.

3. RESULTS AND DISCUSSION

3.1. Feasibility of the PA−PC Spatial Division Platform. In order to verify the feasibility of the photocathode and photoanode synergistic enhancement of the signal amplification strategy, the photocurrent response test was carried out. It was observed that the photocurrent response of the PbS photocathode (Figure 1B, curve a) was much smaller than that

https://doi.org/10.1021/acsami.1c08416
ACS Appl. Mater. Interfaces 2021, 13, 35389−35396

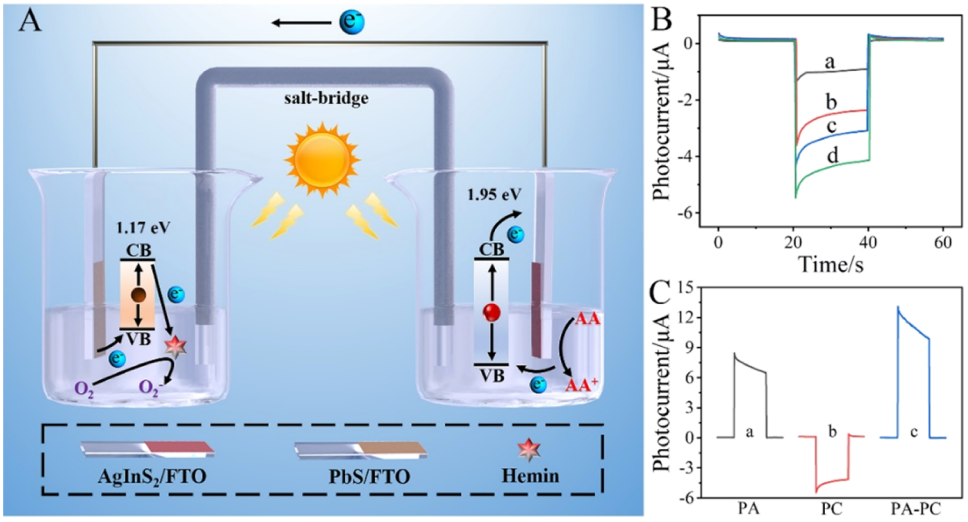

Figure 1. (A) Schematic illustration of the cathode−anode spatial division PEC platform. (B) Photocurrent responses of the PbS QDs in the absence (a) and presence of 0.1 μmol/L (b), 1.0 μmol/L (c), and 10 μmol/L (d) of hemin. (C) Photocurrent responses of the PEC platforms: (a) photoanode (PA, $AgInS_2$ as the photoanode and blank FTO as the photocathode), (b) photocathode (PC, PbS as the photocathode and blank FTO as the photoanode), (c) photoanode−photocathode (PA−PC, $AgInS_2$ as the photoanode and PbS as the photocathode).

Scheme 1. Schematic Illustration of Cathode−Anode Spatial Division PEC Biosensor Based on the One-Step DNA Walker Amplification for Detection of miRNA-21

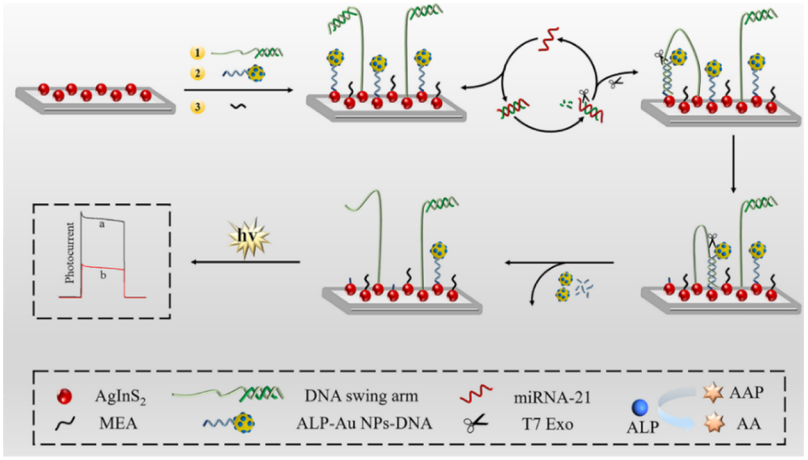

of the $AgInS_2$ photoanode without other modifications. It may cause errors in the strategy verification process. When hemin was added to the photocathode buffer solution (0.1 M Tris−HCl, pH 7.4), the photocurrent response of the PbS photocathode increased significantly, and the cathodic photocurrent gradually increased to the same scale as the $AgInS_2$ photoanode with the increase of hemin concentration (Figure 1B, curve b-d). Subsequently, the feasibility of the cathode- and anode-division photovoltaic platform was verified. As shown in Figure 1C, curve a and curve b represented the photocurrent response of the single $AgInS_2$ photoanode and PbS photocathode, respectively. Excitingly, when the $AgInS_2$ photoanode and PbS photocathode were combined to form a PA−PC (curve c) platform, the photocurrent response was greatly improved, which proved the successful construction of the cathode- and anode-division PEC platform. It was worth mentioning that the anti-interference ability of the PEC biosensor based on this platform took a huge leap because the PEC conversion and sensor recognition process of the two electrodes were partitioned.

The mechanism of the signal amplification strategy that the photocathode and photoanode enhanced synergistically is shown in Figure 1A. Under suitable illumination, both the $AgInS_2$ photoanode and PbS photocathode could be excited to generate electron−hole pairs. For the $AgInS_2$ photoanode (the band gap is 1.95 eV),[17] the photogenerated electrons transitioned from the valence band (VB) to conduction band (CB) and then transferred to the surface of FTO. At the same time, the generated holes were captured by the electron donor [ascorbic acid (AA)] in the solution. For the PbS photocathode (the band gap is 1.17 eV),[20] the photogenerated electrons transitioned from the VB to CB and then transferred to the electron acceptor (hemin) in the solution. Meanwhile, the generated holes were captured by the electrons on the surface of FTO. Hemin(III) was reduced to hemin(II) after accepting electrons, and hemin(II) easily reacted with dissolved oxygen in the solution to regenerated hemin(III) by reducing oxygen.[36] When the two photoelectrodes were in a loop, the photogenerated electrons generated by the $AgInS_2$ photoanode and the photogenerated holes on the PbS

https://doi.org/10.1021/acsami.1c08416
ACS Appl. Mater. Interfaces 2021, 13, 35389−35396

photocathode attracted each other, leading to ultrafast electron transfer and effectively inhibit carrier recombination.[37,38] Under the influence of two-electrode synergistic enhancement, a larger and more stable photocurrent was obtained. The successful construction of the cathode- and anode-division photovoltaic platform provided a new idea for the PEC biosensor, which might have a great application prospect.

3.2. Design of the PEC Biosensor. Here, a PEC biosensor was proposed based on the cathode−anode synergistic enhancement strategy using one-step DNA walker amplification to detect miRNA-21 on the PA−PC division platform. The detection mechanism is shown in Scheme 1. Initially, according to the length of the chain, DNA swing arms and ALP-Au NPs-DNA were sequentially immobilized on the surface of FTO modified by MPA-capped $AgInS_2$ NPs and blocked with MEA. The DNA swing arm was composed of long-strand DNA2 and short-strand DNA1 through complementary base pairing, forming a locked state to limit the hybridization of DNA2 and DNA of ALP-Au NP−DNA on the electrode. Interestingly, when the target miRNA-21 was introduced into the system, miRNA-21 recognized DNA1 and recombined into a more stable double-stranded structure, while the unlocked DNA2 easily hybridized with the DNA of ALP-Au NP−DNA on the surface of the FTO. Meanwhile, under the catalysis of T7 Exo coexisting in the reaction solution, the nucleotides in the blunt or concave 5′ termini of RNA/DNA hybrids were gradually removed, and the released miRNA-21 could combine with another uncut DNA1 to realize the recycling of the target. As expected, the chain type of DNA2 hybridized with DNA of ALP-Au NP−DNA could also trigger the directional cutting of T7 Exo, and the walking strand DNA2 was liberated and bound to other complete DNA of ALP-Au NP−DNA to achieve the DNA walker amplification strategy. Since ALP could catalyze the ascorbic acid 2-phosphate (AAP) in the solution to produce AA that acted as the electron donor, along with DNA walker cycle amplification, more and more ALP was detached from the electrode surface and lost its catalytic ability, eventually resulting in a significant decrease in photocurrent response. As shown in Figure S4, the whole DNA walker amplification response process was confirmed by native polyacrylamide gel electrophoresis. In addition, the transmission electron microscopy (TEM) characterization of ALP-Au NP−DNA before and after enzyme cleavage proved that DNA attached onto Au NPs can be digested by T7 Exo (Figure S5). Therefore, the designed PEC biosensor based on two-electrode synergistic enhancement and one-step DNA walker double amplification strategy provided a novel approach for miRNA-21 high-sensitivity detection and was expected to be applied to clinical diagnosis.

3.3. Characterization of $AgInS_2$ NPs. As shown in the scanning electron microscopy (SEM) image (Figure 2A) and the TEM image (Figure 2B), it was observed that the synthesized $AgInS_2$ NPs were uniform in size and well dispersed, approximately spherical, with an average diameter of 15 nm. High-resolution TEM (HRTEM) was implemented to further clarify the structure and crystallinity of $AgInS_2$ NPs. As shown in Figure S1, the spherical $AgInS_2$ NPs had a clear structure and high crystallinity. Moreover, the lattice spacing of 0.335 nm corresponded to the (002) plane of orthorhombic $AgInS_2$ NPs. In order to explore the optical properties of $AgInS_2$ NPs, ultraviolet−visible (UV−vis) absorption and Fourier transform infrared (FTIR) spectroscopy were carried

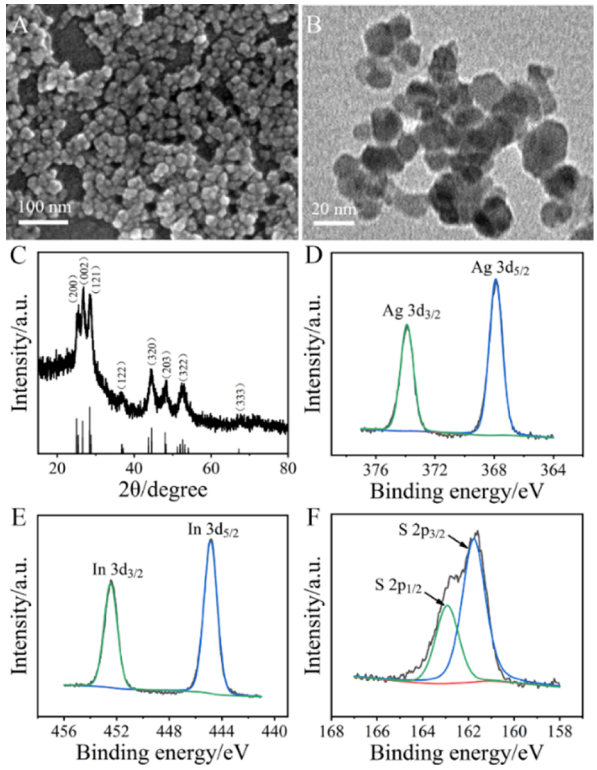

Figure 2. (A) SEM image of $AgInS_2$ NPs. (B) TEM image of $AgInS_2$ NPs. (C) X-ray diffraction (XRD) pattern of $AgInS_2$ NPs. High-resolution XPS spectra of (D) Ag 3d, (E) In 3d, and (F) S 2p of $AgInS_2$ NPs.

out. As shown in Figure S2A, $AgInS_2$ NPs exhibited a characteristic acromion absorption peak at ∼590 nm[39] and the wide absorption spectrum of 400 to 800 nm, making it possible to use almost the entire visible-light region. The peaks located at 3420, 1715, and 1390 cm^{-1} could be assigned to the infrared stretching vibration absorption of O−H, C═O, and C−O,[16] indicating the attachment of carboxyl groups on $AgInS_2$ NPs, which was beneficial to the subsequent biological chain connection (Figure S2B).

Aiming at obtaining and confirming the bulk structure information of $AgInS_2$ NPs, XRD characterization was performed. As displayed in Figure 2C, the diffraction peaks of $AgInS_2$ NPs highly corresponded to JCPDS PDF 25-1328 and were consistent with the previous study, which were a typical orthorhombic system.[39] X-ray photoelectron spectroscopy (XPS) was adopted to qualitatively analyze the elemental composition of $AgInS_2$ NPs. Obviously, the XPS survey scan (Figure S2C) indicated that the obtained $AgInS_2$ NPs did indeed contain Ag, In, and S elements.[40] Figure 2D showed two evident peaks at 367.9 and 373.9 eV, which could be assigned to Ag $3d_{5/2}$ and Ag $3d_{3/2}$. Figure 2E displayed two visible peaks at 444.85 and 452.45 eV belonging to In $3d_{5/2}$ and In $3d_{3/2}$. Furthermore, Figure 2F illustrated two peaks with similar binding energies at 161.77 and 162.93 eV, ascribed to S $2p_{3/2}$ and S $2p_{1/2}$ (doublet splitting of 1.16 eV), respectively.

3.4. Characterization of PbS QDs. According to the TEM image (Figure 3A), the average diameter of the spherical PbS QDs was around 4 nm. As shown in Figure 3B, the HRTEM image of a unitary PbS QD proved good crystallinity, and the lattice spacing was 0.297 nm, corresponding to the (200) plane of cubic PbS. Furthermore, in order to confirm the

https://doi.org/10.1021/acsami.1c08416
ACS Appl. Mater. Interfaces 2021, 13, 35389−35396

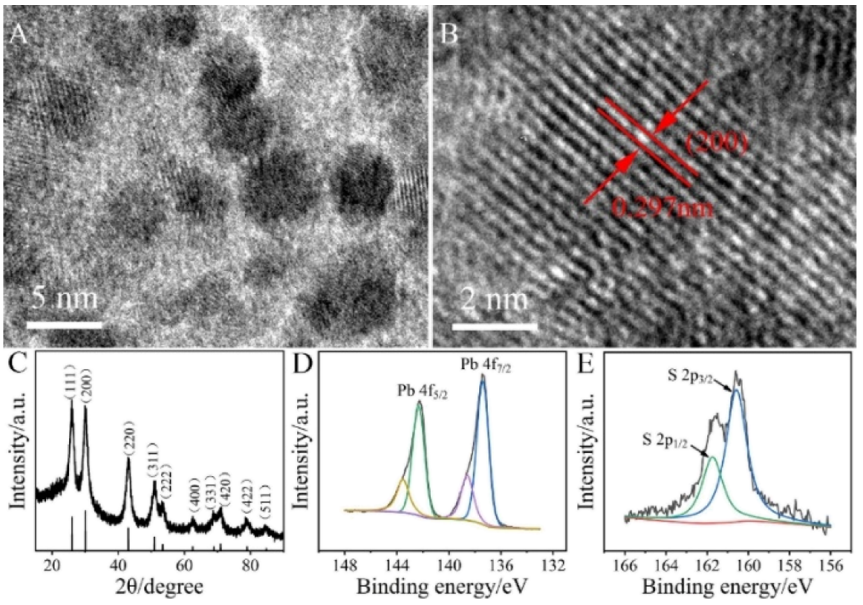

Figure 3. (A) TEM image of PbS QDs. (B) HRTEM image of PbS QDs. (C) XRD pattern of PbS QDs. High-resolution XPS spectra of (D) Pb 4f and € S 2p of PbS QDs.

crystal structure of the PbS QDs, the XRD pattern is displayed (Figure 3C). Comparing with JCPDS PDF 05-0592, it was found that the scattering angles (2θ) of different acuminate diffraction peaks corresponded to the crystal-plane scattering angles of typical face-centered cubic PbS.[20] The UV−vis absorption chart indicated that the PbS QDs were monitored in a wide wavelength range from 400 to 1300 nm (Figure S3A), which proved that it could even use most of the near-infrared light. In the FTIR spectrum (Figure S3B), the presence of characteristic peaks at 3432 cm^{-1} (O−H), 1621 cm^{-1} (C═O) and 1410 cm^{-1} (C−O) demonstrated that the carboxyl group had been successfully modified to the PbS QDs surface.[41] In order to further verify the elemental composition of PbS QDs, XPS was used to characterize it. As shown in Figure 3D, the signature points of Pb at 137.39 and 142.33 eV were ascribed to Pb $4f_{7/2}$ and Pb $4f_{5/2}$ of PbS QDs. Furthermore, broad peaks around 138.59 and 143.53 eV were observed, indicating the formation of the Pb−TGA complex.[41] The coating of TGA might make the material more hydrophilic and biocompatible. The peaks at 160.58 and 161.74 eV resulting from the S $2p_{3/2}$ and S $2p_{1/2}$ could be observed for PbS QDs (Figure 3E). The peak locations of all of the elements are displayed in Figure S3C.[42]

3.5. Characterization of the PEC Biosensor. The $AgInS_2$ photoanode was selected as the platform for carrying the DNA walker, and the PbS photocathode was used to amplify the PEC signal (Figure 4A). The results of PEC and electrochemical impedance spectroscopy (EIS) indicated that the PEC sensor for detecting miRNA-21 was successfully fabricated (Figure 4B,C) (for details, see Supporting Information). In the sensing process, the expression of miRNA-21 concentration in the form of photocurrent response depended on the catalytic effect of ALP on AAP. Therefore, keeping other conditions unchanged, AAP was used to replace AA (0.1 M, pH 7.4) for testing. When ALP-Au NP−DNA was immobilized on the surface of FTO and blocked with MEA, the abundant ALP on the conjugate could catalyze the formation of AA from AAP in the buffer solution, which could provide electrons to inhibit the recombination of photo-

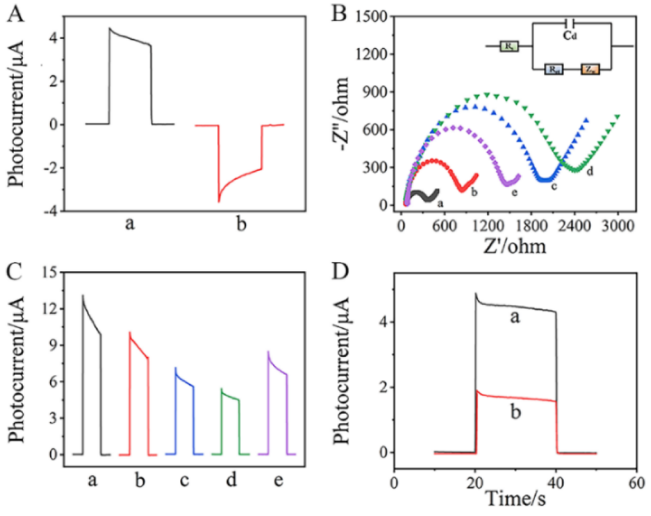

Figure 4. (A) Photocurrent responses of pre-experiment on PEC platforms: (a) the biological steps are mounted on the $AgInS_2$ photoanode or (b) PbS photocathode. (B) EIS in 5 mM $[Fe(CN)_6]^{3-/4-}$ (equimolar amounts of ferrocyanide and ferricyanide) solution containing 0.1 M KCl at a bias potential of 0.19 V and (C) photocurrent responses in PBS solution (0.1 M, pH 7.4) containing 0.1 M AA of (a) $AgInS_2$−FTO, (b) DNA swing arm/$AgInS_2$−FTO, (c) ALP-Au NP−DNA/DNA swing arm/$AgInS_2$−FTO, (d) MEA/ALP-Au NP−DNA/DNA swing arm/$AgInS_2$−FTO and (e) after reaction/MEA/ALP-Au NPs−DNA/DNA swing arm/$AgInS_2$−FTO. (D) Photocurrent responses of (a) MEA/ALP-Au NP−DNA/DNA swing arm/$AgInS_2$−FTO and (b) after reaction/MEA/ALP-Au NP−DNA/DNA swing arm/$AgInS_2$−FTO in PBS solution containing 0.1 M AAP. The concentration of miRNA-21 was 100 nM.

generated electron−hole pairs, thereby significantly enhancing the photocurrent response (Figure 4D, curve a). However, after incubating the modified electrode with a reaction solution containing 100 nM miRNA-21, the unlocked DNA swing arm was complementarily paired with ALP-Au NP−-DNA, thereby activating T7 Exo to release the immobilized ALP-Au NP−

https://doi.org/10.1021/acsami.1c08416
ACS Appl. Mater. Interfaces 2021, 13, 35389−35396

DNA. The ALP entering the solution from the surface of the electrode lost its ability to catalyze the formation of AA from AAP, making the system devoid of electron donors. Compared with steric hindrance, the electron donor had a more direct impact on the PEC system, which led to a significant reduction in the photocurrent response (Figure 4D, curve b). The change of photocurrent in line with expectations proved that the designed PEC biosensor was potential.

3.6. Detection of miRNA-21. In order to evaluate the sensitivity of the proposed biosensor for miRNA-21 analysis, the PEC examination was performed under optimal conditions by changing the target concentration. As shown in Figure 5A,

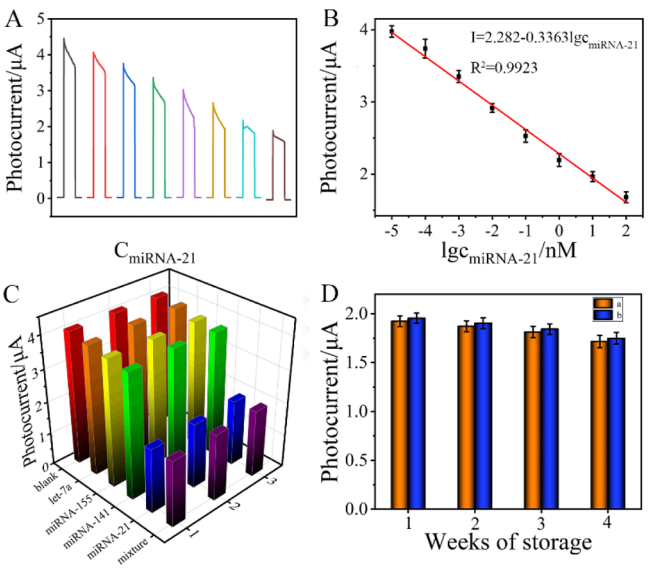

Figure 5. PEC detections were implemented in 0.1 M AAP (PBS pH 7.4). (A) Photocurrent responses of different miRNA-21 concentrations (10 fM, 100 fM, 1 pM, 10 pM, 100 pM, 1 nM, 10 nM, and 100 nM from left to right). (B) Logarithm of the PEC responses relative to the miRNA-21 concentration. (C) Selectivity of the biosensor toward different targets: blank, 100 nM let-7a, 100 nM miRNA-155, 100 nM miRNA-141, 10 nM miRNA-21, and the miRNA mixture including target miRNA-21. (D) Stability of the proposed PEC biosensor (10 nM miRNA-21) at room temperature (a) and in the freezer (b).

with the miRNA-21 concentration increasing from 10 fM to 100 nM, the corresponding photocurrent response decreased continuously, thus establishing a functional relationship between the logarithm of the target concentration and the photocurrent data. Figure 5B displays that the well-fitted linear regression equation was $I = -0.3363 \log c + 2.282$ with its correlation coefficient of $R^2 = 0.9923$. Moreover, in the case of a signal-to-noise ratio of 3, the detection limit reached 3.4 fM. Referring to other types of miRNA sensors (Table S2), the designed PEC biosensor possessed a wide working range and low detection limit and could achieve high efficiency and sensitive detection of miRNA-21, which had potential application values in biological analysis and disease monitoring.

3.7. Selectivity, Reproducibility, and Stability of the PEC Biosensor. The anti-interference ability of the biosensor could largely determine the accuracy of detection results. Under the optimized experimental conditions, let-7a, miRNA-155, and miRNA-141 were chosen as possible interferants to replace miRNA-21 to estimate the selectivity of the PEC biosensor. As shown in Figure 5C, although the sequences of miRNA-141, miRNA-155, and let-7a were highly like miRNA-21, they did not unlock the DNA swing arm to trigger the DNA walker. Hence, the PEC response was similar to the blank component. In sharp contrast, the addition of 10 nM miRNA-21 or the miRNAs mixture including target 10 nM miRNA-21caused the obvious photocurrent attenuation, proving that the biosensor had excellent selectivity. Reproducibility was an important indicator to evaluate a biosensor; hence, 10 times consecutive "on/off" PEC tests were conducted under the irradiation of xenon lamps. Figure S7 reveals that the photocurrent of the prepared biosensor had only slight fluctuations with the relative standard deviation (RSD) of 2.42%, showing prominent reproducibility. The developed PEC biosensor was also placed in an environment of 25 and 4 °C for 1 month to investigate its stability with temperature and time. Measured once a week, the obtained photocurrent response remained stable both at room temperature or in the refrigerator, indicating that the PEC biosensor with good stability could be employed for a long time (Figure 5D).

3.8. Application of the Cathode−Anode Spatial-Division PEC Biosensor. To evaluate the feasibility of the cathode−anode spatial-division PEC sensing system in the detection of real complex samples, the recovery of different concentrations of target miRNA-21 (0.1, 1, 10, 100, and 1000 pM) spiked in diluted human serum samples (acquired from Shandong Cancer Hospital, China) was experimented. As displayed in Table S3, the recovery values obtained in the test were between 95.1 and 103.4% and the corresponding RSD values were 2.5−4.1%, which proved that even if there was interference from complex biological media, the constructed miRNA-21 biosensor could maintain accuracy and reliability. Based on the excellent performance of such a biosensor, it could provide a strong guarantee for early clinical diagnosis.

4. CONCLUSIONS

Using the red light-sensitive $AgInS_2$ photoanode and the near-infrared-absorbable PbS photocathode with high PEC activity and biocompatibility, a cathode−anode spatial division PEC platform based on the two-electrode synergistic amplification strategy was successfully constructed. Compared with the traditional single anode or cathode PEC sensor, the designed one possessed two obvious advantages simultaneously. First, both photoelectrodes can be excited and promoted by each other, which obtained a considerable photocurrent response to promote the sensitivity of detection. Second, the spatial division of two photoelectrodes could avoid the cross-talk of reactions on the surface of the electrode and the error caused by the interference components in the complex biological sample, which greatly improved the selectivity of detection. Furthermore, by performing one-step DNA walker amplification on the $AgInS_2$ photoanode, the constructed PEC biosensor can accomplish target cycling and enzymatic digestion, and it extremely simplified the operation steps. Therefore, under the dual amplification strategy of cathode−anode synergistic enhancement and one-step DNA walker amplification, the PEC biosensor realizes the ultrasensitive detection of miRNA-21, which has great potential for early clinical diagnosis application.

https://doi.org/10.1021/acsami.1c08416
ACS Appl. Mater. Interfaces 2021, 13, 35389−35396

■ ASSOCIATED CONTENT

Supporting Information

The Supporting Information is available free of charge at https://pubs.acs.org/doi/10.1021/acsami.1c08416.

Materials and apparatus, characterization of $AgInS_2$ NPs, characterization of PbS QDs, condition optimization and photoelectrochemical characterization of the prepared photoelectrochemical biosensor, and comparison of different methods for miRNA detection (PDF)

■ AUTHOR INFORMATION

Corresponding Author

Shenguang Ge − *Institute for Advanced Interdisciplinary Research, University of Jinan, Jinan 250022, P.R. China;* orcid.org/0000-0002-0537-6491; Email: chm_gesg@163.com

Authors

Chuan Huang − *Institute for Advanced Interdisciplinary Research, University of Jinan, Jinan 250022, P.R. China*

Yunqing Liu − *Institute for Advanced Interdisciplinary Research, University of Jinan, Jinan 250022, P.R. China*

Yina Sun − *Institute for Advanced Interdisciplinary Research, University of Jinan, Jinan 250022, P.R. China*

Fengyi Wang − *Institute for Advanced Interdisciplinary Research, University of Jinan, Jinan 250022, P.R. China*

Jinghua Yu − *School of Chemistry and Chemical Engineering, University of Jinan, Jinan 250022, P.R. China;* orcid.org/0000-0001-5043-0322

Complete contact information is available at: https://pubs.acs.org/10.1021/acsami.1c08416

Author Contributions

§C.H. and Y.L. contributed equally to this work.

Notes

The authors declare no competing financial interest.

■ ACKNOWLEDGMENTS

This work was supported by the National Natural Science Foundation of China (22074053, 21775055, and 21874055), Excellent Youth Innovation Team in the Universities of Shandong (2019KJC016), The Project of "20 items of University" of Jinan (2020GXRC047 and 2018GXRC001), the Taishan Scholars Program, and Case-by-Case Project for Top Outstanding Talents of Jinan.

■ REFERENCES

(1) Saliminejad, K.; Khorram Khorshid, H. R.; Soleymani Fard, S.; Ghaffari, S. H. An Overview of MicroRNAs: Biology, Functions, Therapeutics, and Analysis Methods. *J. Cell. Physiol.* **2019**, *234*, 5451−5465.

(2) Bhaskaran, M.; Mohan, M. MicroRNAs: History, Biogenesis, and Their Evolving Role in Animal Development and Disease. *Vet. Pathol.* **2014**, *51*, 759−774.

(3) Zhou, Y.; Ren, H.; Dai, B.; Li, J.; Shang, L.; Huang, J.; Shi, X. Hepatocellular Carcinoma-Derived Exosomal MiRNA-21 Contributes to Tumor Progression by Converting Hepatocyte Stellate Cells to Cancer-Associated Fibroblasts. *J. Exp. Clin. Cancer Res.* **2018**, *37*, 324−342.

(4) Yang, K.; Wang, S.; Cheng, Y.; Tian, Y.; Hou, J. Role of MiRNA-21 in the Diagnosis and Prediction of Treatment Efficacy of Primary Central Nervous System Lymphoma. *Oncol. Lett.* **2019**, *17*, 3475−3481.

(5) Zhao, J.; Fu, C.; Huang, C.; Zhang, S.; Wang, F.; Zhang, Y.; Zhang, L.; Ge, S.; Yu, J. Co_3O_4-Au Polyhedron Mimic Peroxidase-And Cascade Enzyme-Assisted Cycling Process-Based Photoelectrochemical Biosensor for Monitoring of MiRNA-141. *Chem. Eng. J.* **2021**, *406*, 126892−126900.

(6) Li, Z.; Yang, H.; Hu, M.; Zhang, L.; Ge, S.; Cui, K.; Yu, J. Cathode Photoelectrochemical Paper Device for MicroRNA Detection Based on Cascaded Photoactive Structures and Hemin/Pt Nanoparticle-Decorated DNA Dendrimers. *ACS Appl. Mater. Interfaces* **2020**, *12*, 17177−17184.

(7) Li, N.; Fu, C.; Wang, F.; Sun, Y.; Zhang, L.; Ge, S.; Zhu, P.; Yu, J. Photoelectrochemical Detection of Let-7a Based on Toehold-Mediated Strand Displacement Reaction and Bi_2S_3 Nanoflower for Signal Amplification. *Sens. Actuators, B* **2020**, *323*, 128655−128662.

(8) Pan, L.; Sun, S.; Chen, Y.; Wang, P.; Wang, J.; Zhang, X.; Zou, J. J.; Wang, Z. L. Advances in Piezo-Phototronic Effect Enhanced Photocatalysis and Photoelectrocatalysis. *Adv. Energy Mater.* **2020**, *10*, 2000214−2000239.

(9) Li, H.; Li, J.; Zhu, Y.; Xie, W.; Shao, R.; Yao, X.; Gao, A.; Yin, Y. Cd^{2+}-Doped Amorphous TiO_2 Hollow Spheres for Robust and Ultrasensitive Photoelectrochemical Sensing of Hydrogen Sulfide. *Anal. Chem.* **2018**, *90*, 5496−5502.

(10) Qian, Y.; Feng, J.; Xu, R.; Fan, D.; Du, Y.; Ren, X.; Wei, Q.; Ju, H. Zinc and Molybdenum Co-Doped $BiVO_4$ Nanoarray for Photoelectrochemical Diethylstilbestrol Analysis Based on the Dual-Competitive System of Manganese Hexacyanoferrate Hydrate Nanocubes. *ACS Appl. Mater. Interfaces* **2020**, *12*, 16662−16669.

(11) Wang, H.-H.; Li, M.-J.; Wang, H.-J.; Chai, Y.-Q.; Yuan, R. P-N-Sensitized Heterostructure Co_3O_4/Fullerene with Highly Efficient Photoelectrochemical Performance for Ultrasensitive DNA Detection. *ACS Appl. Mater. Interfaces* **2019**, *11*, 23765−23772.

(12) Wang, S.; Wang, F.; Fu, C.; Sun, Y.; Zhao, J.; Li, N.; Liu, Y.; Ge, S.; Yu, J. $AgInSe_2$-Sensitized ZnO Nanoflower Wide-spectrum Response Photoelectrochemical/Visual Sensing Platform via Au@Nanorod-Anchored CeO_2 Octahedron Regulated Signal. *Anal. Chem.* **2020**, *92*, 7604−7611.

(13) Li, R.; Tu, W.; Wang, H.; Dai, Z. Near-Infrared Light Excited and Localized Surface Plasmon Resonance-Enhanced Photoelectrochemical Biosensing Platform for Cell Analysis. *Anal. Chem.* **2018**, *90*, 9403−9409.

(14) Song, Z.; Fan, G.-C.; Li, Z.; Gao, F.; Luo, X. Universal Design of Selectivity-Enhanced Photoelectrochemical Enzyme Sensor: Integrating Photoanode with Biocathode. *Anal. Chem.* **2018**, *90*, 10681−10687.

(15) Fan, G.-C.; Lu, Y.; Zhao, H.; Liu, Q.; Li, Z.; Luo, X. Photoelectrochemical Cell Enhanced by Ternary Heterostructured Photoanode: Toward High-Performance Self-Powered Cathodic Cytosensing. *Biosens. Bioelectron.* **2019**, *137*, 52−57.

(16) Li, J.; Lin, X.; Zhang, Z.; Tu, W.; Dai, Z. Red Light-Driven Photoelectrochemical Biosensing for Ultrasensitive and Scatheless Assay of Tumor Cells Based on Hypotoxic $AgInS_2$ Nanoparticles. *Biosens. Bioelectron.* **2019**, *126*, 332−338.

(17) Ganguly, P.; Mathew, S.; Clarizia, L.; Kumar R, S.; Akande, A.; Hinder, S. J.; Breen, A.; Pillai, S. C. Ternary Metal Chalcogenide Heterostructure ($AgInS_2$−TiO_2) Nanocomposites for Visible Light Photocatalytic Applications. *ACS Omega* **2020**, *5*, 406−421.

(18) An, Y.; Tang, L.; Jiang, X.; Chen, H.; Yang, M.; Jin, L.; Zhang, S.; Wang, C.; Zhang, W. A Photoelectrochemical Immunosensor Based on Au-Doped TiO_2 Nanotube Arrays for the Detection of α-Synuclein. *Chem.—Eur. J.* **2010**, *16*, 14439−14446.

(19) Hao, Q.; Wang, P.; Ma, X.; Su, M.; Lei, J.; Ju, H. Charge Recombination Suppression-Based Photoelectrochemical Strategy for Detection of Dopamine. *Electrochem. Commun.* **2012**, *21*, 39−41.

(20) Wang, G.-L.; Shu, J.-X.; Dong, Y.-M.; Wu, X.-M.; Zhao, W.-W.; Xu, J.-J.; Chen, H.-Y. Using G-Quadruplex/Hemin to "Switch-On" the Cathodic Photocurrent of P-Type PbS Quantum Dots: Toward a Versatile Platform for Photoelectrochemical Aptasensing. *Anal. Chem.* **2015**, *87*, 2892−2900.

(21) Yang, H.; Wang, J.; Li, X.; Zhang, L.; Yu, H.; Zhang, L.; Ge, S.; Yu, J.; Zhang, Y. Self-Circulation Oxygen−Hydrogen Peroxide−Oxygen System for Ultrasensitive Cathode Photoelectrochemical Bioassay Using a Stacked Sealed Paper Device. *ACS Appl. Mater. Interfaces* **2021**, *13*, 19793−19802.
(22) Xu, Y.-T.; Yu, S.-Y.; Zhu, Y.-C.; Fan, G.-C.; Han, D.-M.; Qu, P.; Zhao, W.-W. Cathodic Photoelectrochemical Bioanalysis. *TrAC, Trends Anal. Chem.* **2019**, *114*, 81−88.
(23) DuChene, J. S.; Tagliabue, G.; Welch, A. J.; Li, X.; Cheng, W.-H.; Atwater, H. A. Optical Excitation of a Nanoparticle Cu/p-NiO Photocathode Improves Reaction Selectivity for CO_2 Reduction in Aqueous Electrolytes. *Nano Lett.* **2020**, *20*, 2348−2358.
(24) Zhang, L.; Zhu, Y.-C.; Liang, Y.-Y.; Zhao, W.-W.; Xu, J.-J.; Chen, H.-Y. Semiconducting CuO Nanotubes: Synthesis, Characterization, and Bifunctional Photocathodic Enzymatic Bioanalysis. *Anal. Chem.* **2018**, *90*, 5439−5444.
(25) Nair, G.; Chang, L.-Y.; Geyer, S. M.; Bawendi, M. G. Perspective on the Prospects of a Carrier Multiplication Nanocrystal Solar Cell. *Nano Lett.* **2011**, *11*, 2145−2151.
(26) Yang, Y.; Rodríguez-Córdoba, W.; Lian, T. Multiple Exciton Generation and Dissociation in PbS Quantum Dot-Electron Acceptor Complexes. *Nano Lett.* **2012**, *12*, 4235−4241.
(27) Wang, G.-L.; Liu, K.-L.; Dong, Y.-M.; Wu, X.-M.; Li, Z.-J.; Zhang, C. A New Approach to Light up The Application of Semiconductor Nanomaterials for Photoelectrochemical Biosensors: Using Self-Operating Photocathode as a Highly Selective Enzyme Sensor. *Biosens. Bioelectron.* **2014**, *62*, 66−72.
(28) Fan, G.-C.; Shi, X.-M.; Zhang, J.-R.; Zhu, J.-J. Cathode Photoelectrochemical Immunosensing Platform Integrating Photocathode with Photoanode. *Anal. Chem.* **2016**, *88*, 10352−10356.
(29) Zhao, W.-W.; Ma, Z.-Y.; Yan, D.-Y.; Xu, J.-J.; Chen, H.-Y. In Situ Enzymatic Ascorbic Acid Production as Electron Donor for CdS Quantum Dots Equipped TiO_2 Nanotubes: A General and Efficient Approach for New Photoelectrochemical Immunoassay. *Anal. Chem.* **2012**, *84*, 10518−10521.
(30) Wang, F.; Fu, C.; Huang, C.; Li, N.; Wang, Y.; Ge, S.; Yu, J. Paper-Based Closed Au-Bipolar Electrode Electrochemiluminescence Sensing Platform for the Detection of MiRNA-155. *Biosens. Bioelectron.* **2020**, *150*, 111917−111925.
(31) Liu, J.-L.; Tang, Z.-L.; Zhang, J.-Q.; Chai, Y.-Q.; Zhuo, Y.; Yuan, R. Morphology-Controlled 9,10-Diphenylanthracene Nanoblocks as Electrochemiluminescence Emitters for MicroRNA Detection with One-Step DNA Walker Amplification. *Anal. Chem.* **2018**, *90*, 5298−5305.
(32) Peng, R.; Zheng, X.; Lyu, Y.; Xu, L.; Zhang, X.; Ke, G.; Liu, Q.; You, C.; Huan, S.; Tan, W. Engineering a 3D DNA-Logic Gate Nanomachine for Bispecific Recognition and Computing on Target Cell Surfaces. *J. Am. Chem. Soc.* **2018**, *140*, 9793−9796.
(33) Wang, J.; Wang, D.-X.; Tang, A.-N.; Kong, D.-M. Highly Integrated, Biostable, and Self-Powered DNA Motor Enabling Autonomous Operation in Living Bodies. *Anal. Chem.* **2019**, *91*, 5244−5251.
(34) Peng, H.; Li, X.-F.; Zhang, H.; Le, X. C. A MicroRNA-Initiated DNAzyme Motor Operating in Living Cells. *Nat. Commun.* **2017**, *8*, 14378−14391.
(35) Zhao, W.-W.; Ma, Z.-Y.; Yu, P.-P.; Dong, X.-Y.; Xu, J.-J.; Chen, H.-Y. Highly Sensitive Photoelectrochemical Immunoassay with Enhanced Amplification Using Horseradish Peroxidase Induced Biocatalytic Precipitation on a CdS Quantum Dots Multilayer Electrode. *Anal. Chem.* **2012**, *84*, 917−923.
(36) Deng, S.; Cheng, L.; Lei, J.; Cheng, Y.; Huang, Y.; Ju, H. Label-Free Electrochemiluminescent Detection of DNA by Hybridization with a Molecular Beacon to Form Hemin/G-Quadruplex Architecture for Signal Inhibition. *Nanoscale* **2013**, *5*, 5435−5441.
(37) Xin, X.; He, M.; Han, W.; Jung, J.; Lin, Z. Low-Cost Copper Zinc Tin Sulfide Counter Electrodes for High-Efficiency Dye-Sensitized Solar Cells. *Angew. Chem., Int. Ed.* **2011**, *50*, 11739−11742.
(38) Wu, M.; Lin, X.; Wang, Y.; Wang, L.; Guo, W.; Qi, D.; Peng, X.; Hagfeldt, A.; Grätzel, M.; Ma, T. Economical Pt-free Catalysts for Counter Electrodes of Dye-Sensitized Solar Cells. *J. Am. Chem. Soc.* **2012**, *134*, 3419−3428.
(39) Jin, H.; Gui, R.; Wang, Z.; Xia, J.; Yang, M.; Zhang, F.; Bi, S. Retracted Article: Facile fabrication of water-dispersible AgInS2 quantum dots and mesoporous AgInS2 nanospheres with visible photoluminescence. *RSC Adv.* **2015**, *5*, 68287−68292.
(40) Kobosko, S. M.; Jara, D. H.; Kamat, P. V. $AgInS_2$-ZnS Quantum Dots: Excited State Interactions with TiO_2 and Photovoltaic Performance. *ACS Appl. Mater. Interfaces* **2017**, *9*, 33379−33388.
(41) Yu, Y.; Zhang, K.; Sun, S. One-Pot Aqueous Synthesis of Near Infrared Emitting PbS Quantum Dots. *Appl. Surf. Sci.* **2012**, *258*, 7181−7187.
(42) Zhang, H.; Gao, Y.; Zhu, G.; Li, B.; Gou, J.; Cheng, X. Synthesis of PbS/TiO_2 Nano-Tubes Photoelectrode and its Enhanced Visible Light Driven Photocatalytic Performance and Mechanism for Purification of 4-Chlorobenzoic Acid. *Sep. Purif. Technol.* **2019**, *227*, 115697−115704.

https://doi.org/10.1021/acsami.1c08416
ACS Appl. Mater. Interfaces 2021, 13, 35389−35396